CrossMark

Data-driven MHD Simulation of Successive Solar Plasma Eruptions

Takafumi Kaneko , Sung-Hong Park , and Kanya Kusano
Institute for Space-Earth Environmental Research, Nagoya University, Furo-cho, Chikusa-ku, Nagoya, Aichi, 464-8601, Japan; kaneko@isee.nagoya-u.ac.jp

Abstract

Solar flares and plasma eruptions are sudden releases of magnetic energy stored in the plasma atmosphere. To understand the physical mechanisms governing their occurrences, three-dimensional magnetic fields from the photosphere up to the corona must be studied. The solar photospheric magnetic fields are observable, whereas the coronal magnetic fields cannot be measured. One method for inferring coronal magnetic fields is performing data-driven simulations, which involves time-series observational data of the photospheric magnetic fields with the bottom boundary of magnetohydrodynamic simulations. We developed a data-driven method in which temporal evolutions of the observational vector magnetic field can be reproduced at the bottom boundary in the simulation by introducing an inverted velocity field. This velocity field is obtained by inversely solving the induction equation and applying an appropriate gauge transformation. Using this method, we performed a data-driven simulation of successive small eruptions observed by the Solar Dynamics Observatory and the Solar Magnetic Activity Telescope in 2017 November. The simulation well reproduced the converging motion between opposite-polarity magnetic patches, demonstrating successive formation and eruptions of helical flux ropes.

Supporting material: animation

1. Introduction

Solar flares are the sudden releases of energy from the Sun. Flares are often accompanied by plasma eruptions such as prominence eruptions and coronal mass ejections. Flares and plasma eruptions are caused by the release of magnetic energy stored in the plasma atmosphere. Evidences of flares and plasma eruptions have also been found in other Sun-like stars (Osten et al. 2005; Pandey & Singh 2008; Maehara et al. 2012; Notsu et al. 2019; Namekata et al. 2020). The Sun is the only star for which the photospheric magnetic fields can be observed with a high spatio-temporal resolution. From the solar observations and theoretical studies based on magnetohydrodynamic (MHD) theories, we can infer the detailed magnetic activities leading to the sudden energy release, which can be common in other Sun-like stars. In the current understanding of solar physics, magnetic reconnection and MHD instabilities (Hood & Priest 1979; Kliem & Török 2006; Ishiguro & Kusano 2017) are the essential mechanisms leading to the magnetic energy release.

In the solar observations, the photospheric magnetic fields are temporally changed via advection by convective flows and magnetic fluxes emerging from the deeper convection zone. To reveal the mechanisms of the explosive events and develop methodologies to predict them, previous studies attempted to evaluate the possibility of magnetic reconnection and the critical conditions of MHD instabilities (Amari et al. 2014; Kusano et al. 2020). For this, the information of three-dimensional magnetic fields from the photosphere up to the corona is required. The photospheric magnetic fields can be observed, whereas the coronal magnetic fields cannot be measured directly. Previous studies developed numerical methods to extrapolate three-dimensional coronal magnetic fields from the two-dimensional observational vector magnetic fields in the photosphere, e.g., nonlinear force-free field

(NLFFF) approximation (reviewed by Inoue 2016). There have been attempts of data-constrained simulations, where the NLFFF approximation was used as the initial condition of MHD simulation (Amari et al. 2014; Muhamad et al. 2017). In these simulations, the photospheric magnetic fields after temporal integration did not always reproduce the observed ones. Another attempt was the data-driven simulation in which time-series photospheric magnetic data were involved in the bottom boundary of MHD simulations. The expected advantage of the data-driven methods, compared with the NLFFF or data-constrained model, is that the results are free from the assumption of force-free field. We can follow more realistic temporal evolution of coronal magnetic fields as a response of temporal change of the observational photospheric magnetic fields. Several data-driven MHD simulations have been performed, and their results agree with some aspects in the observations, e.g., morphology of the coronal magnetic loops (Cheung & DeRosa 2012; Cheung et al. 2015; Jiang et al. 2016; Hayashi et al. 2018, 2019; Guo et al. 2019; Pomoell et al. 2019; He et al. 2020). In contrast, a recent comparative study by Toriumi et al. (2020) reported that the numerical solutions obtained from the different data-driven simulations using the same time-series magnetic data were different from each other. The data-driven methods must be improved further to resolve these discrepancies.

In this study, we focus on the velocity fields in the bottom boundary of MHD simulation. In several data-driven methods, the velocity fields at the bottom boundary were set to be zero, leading to physical inconsistency between velocity fields and electric or magnetic fields in terms of the induction equation. A recent study by Hayashi et al. (2019) combined the velocity fields derived from a differential affine velocity estimator for vector magnetograms (DAVE4VM; Schuck 2006) with their own data-driven method (denoted as the *v*-driven method in
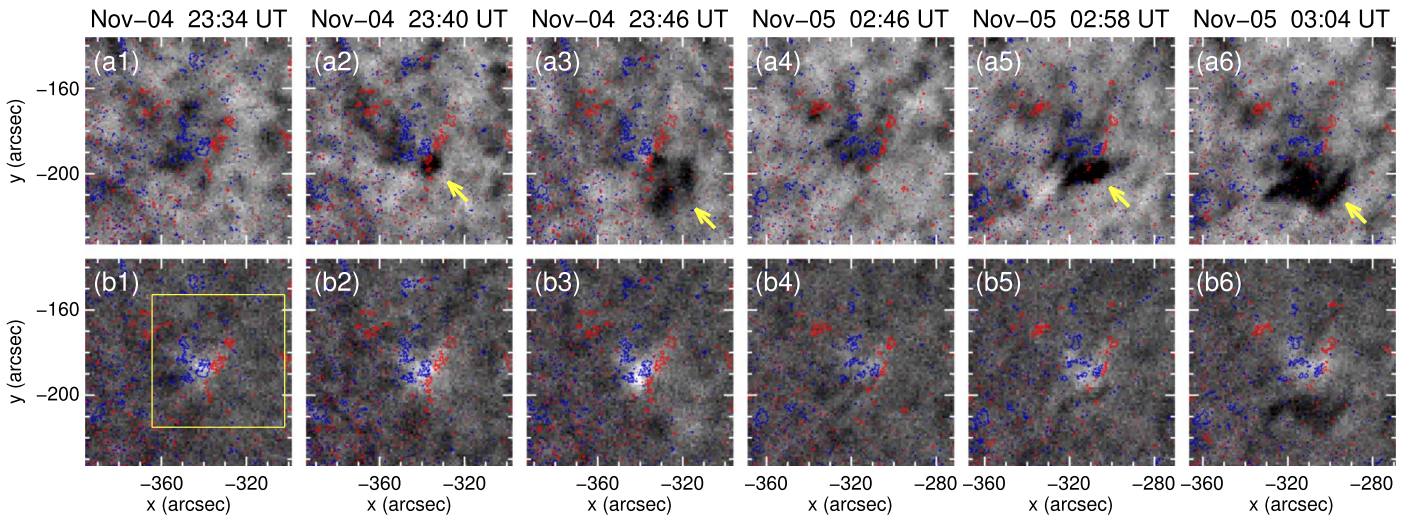
Figure 1. Two successive eruption events observed in Hα − 0.5 Å images (top panels) and Hα line center images (bottom panels). The arrows in panels (a2) and (a3) indicate the first event, while those in panels (a5) and (a6) indicate the second event. In each panel, the red and blue contours represent ±50 G of the vertical magnetic field B_z. The yellow box in panel (b1) represents the region used as the bottom boundary in our MHD simulation.

their paper). They confirmed that the frozen-in condition between plasmas and magnetic fields was well established. This is because the DAVE4VM-inferred velocity works as the bottom boundary condition to the equation of motion in MHD simulation, providing the motion of plasmas coherent with the time evolution of the magnetic fields in the observation. Another recent study by Guo et al. (2019) reported that the numerical results of data-driven simulations with and without velocity fields by DAVE4VM were similar in terms of morphology and propagation path of the erupted flux ropes. They argued that eruption inevitably happens if the initial condition of MHD simulation is already close to the dynamic eruptive phase. Their conclusion was that the change of the bottom boundary condition had a subtle effect on the onset mechanism, while it would affect magnetic energy buildup before the eruptive phase. Since the observational targets and many aspects of numerical techniques were different in Hayashi et al. (2019) and Guo et al. (2019), it is fairly difficult to compare their results. One issue of concern about their numerical techniques is that the DAVE4VM-inferred velocity is not always consistent with the inverted electric fields or the time evolution of the observational magnetic fields used as the bottom boundary condition of MHD simulations. In the present study, we attempted to implement an inversion technique of the induction equation directly in our simulation code, and we proposed a method to derive the velocity fields reproducing the observed time evolution of the magnetic field as a numerical solution of MHD equations. To confirm the feasibility of the method, we applied it to the successive small eruptive events that occurred in 2017 November.

The observations of the eruptive events are described in Section 2. The numerical method including velocity inversion is described in Section 3. The numerical results are shown in Section 4. We summarize and discuss the results in Section 5.

2. Observation

The Solar Dynamics Doppler Imager (SDDI; Ichimoto et al. 2017) installed on the Solar Magnetic Activity Research Telescope (SMART; Ueno et al. 2004) at Hida Observatory of Kyoto University provides full-disk solar images at multiple wavelengths around the Hα λ6563 line with a 0.25 Å bandpass. The top and bottom panels of Figure 1 show Hα blue wing images at −0.5 Å from the line center and Hα line center images, respectively, in six snapshots taken from SMART/ SDDI observations on 2017 November 4–5, which demonstrate two successive eruptions. As indicated by the arrow in panel (a2) of Figure 1, the first eruption event started at 23:40 UT on November 4 and appeared as a compact dark feature with a size of ∼10″ in Hα − 0.5 Å. This dark feature (i.e., a so-called Hα upflow event), which is only visible in the Hα blue wing, displays an upward motion and is known to be often associated with magnetic reconnection (Chae et al. 1998; Wang et al. 1998). In a sequence of Hα − 0.5 Å images, it was found that the Hα − 0.5 Å upflow features increase in size as they erupt in the southwest direction (see panel (a3)). During the eruption, an enhanced brightening in Hα was observed near the magnetic polarity inversion line (PIL), where two opposite-polarity magnetic patches approached each other. Approximately 3 hr after the first eruption, another eruption event began at 02:50 UT on November 5, exhibiting characteristics similar to those of the first eruption event in the context of the southwest eruption direction and Hα brightening. In the case of the second eruption, contrarily, we note that an inverse S-shaped structure is clearly seen in the Hα line center (refer to panel (b6)).

In this study, we used a sequence of photospheric vector magnetograms obtained in a 12-minute cadence by the Helioseismic and Magnetic Imager (HMI; Schou et al. 2012) on board the Solar Dynamics Observatory (SDO; Pesnell et al. 2012). The pixel size of the HMI vector magnetograms was ∼360 km. Figure 2 shows two co-aligned images of the vertical (B_z) and horizontal (B_x and B_y) components of the photospheric magnetic field at 22:58 UT on 2017 November 4 (left column) and at 00:58 UT on 2017 November 5 (right column). The field of view of the co-aligned magnetic field images is marked by the yellow box in panel (b1) of Figure 1, which contains the magnetic source region that produced the two eruptions. The source region consists of two main opposite-polarity magnetic patches that, in general, showed a converging motion, as well as a decrease in the magnetic flux of both polarities over a 5 hr interval around the times that the two eruptions occurred.
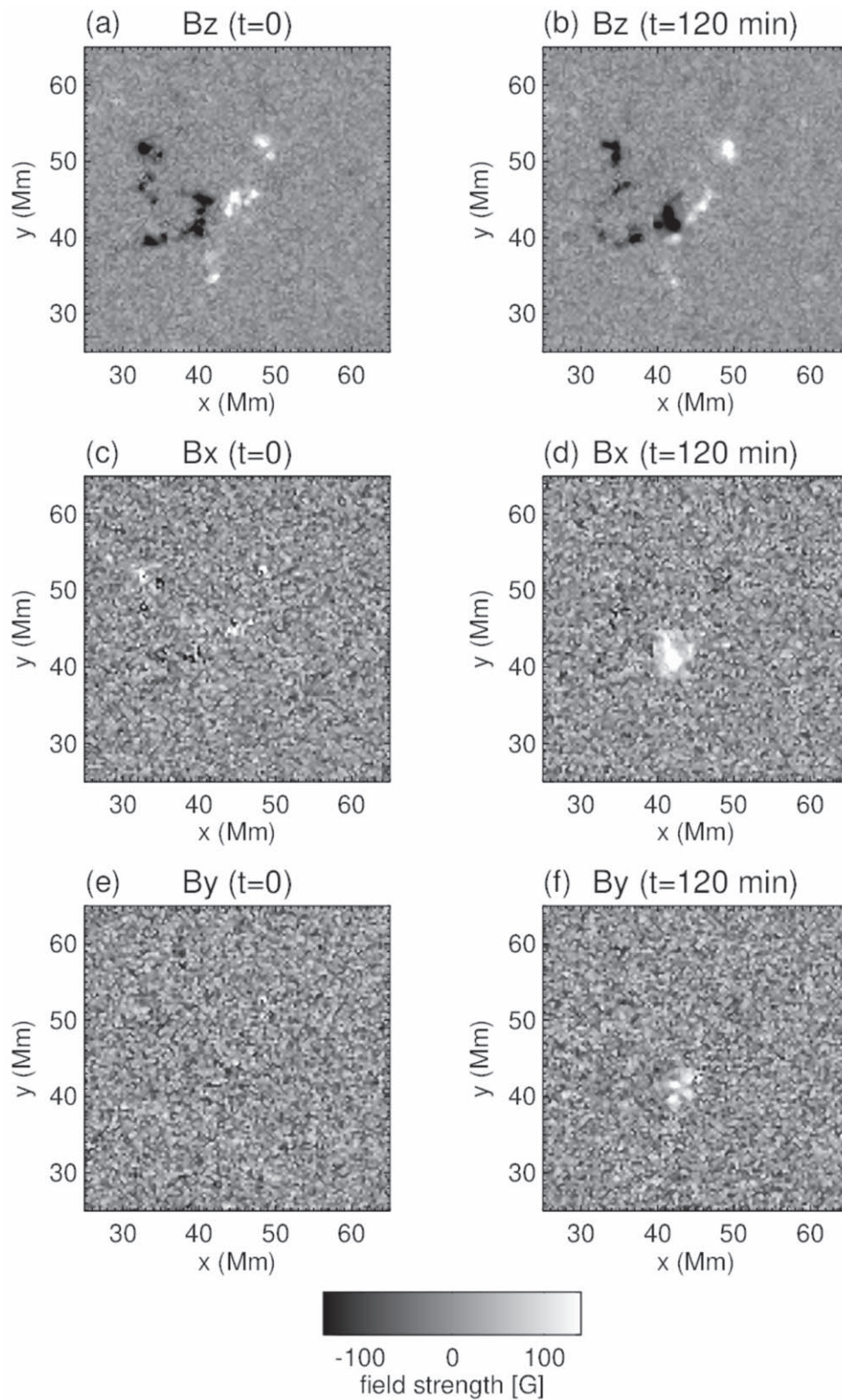
Figure 2. Snapshots of time-series data of magnetic field observed by SDO/HMI. Panels (a), (c), and (e) show snapshots of 22:58 UT on 2017 November 4 (corresponding to $t = 0$ in the simulation). Panels (b), (d), and (f) show snapshots of 00:58 UT on 2017 November 5 (corresponding to $t = 120$ minutes in the simulation). The field of view of these figures is represented by the yellow box in Figure 1(b1).

Moreover, as shown in panels (d) and (f) of Figure 2, the strengths of the horizontal components B_x and B_y are found to increase after the first eruption.

3. Numerical Method

We numerically solved the zero-beta MHD equations as follows:

$$\frac{\partial \rho}{\partial t} + \nabla \cdot (\rho \boldsymbol{v}) = 0, \tag{1}$$

$$\frac{\partial (\rho \boldsymbol{v})}{\partial t} + \nabla \cdot \left(\rho \boldsymbol{v}\boldsymbol{v} + \frac{B^2}{8\pi}\boldsymbol{I} - \frac{\boldsymbol{B}\boldsymbol{B}}{4\pi} \right) = 0, \tag{2}$$

$$\frac{\partial \boldsymbol{B}}{\partial t} = \nabla \times (\boldsymbol{v} \times \boldsymbol{B} - \eta \boldsymbol{J}), \tag{3}$$

$$\boldsymbol{J} = \frac{1}{4\pi}\nabla \times \boldsymbol{B}, \tag{4}$$

where t, ρ, $\boldsymbol{v}$, $\boldsymbol{B}$, $\boldsymbol{J}$, η, and $\boldsymbol{I}$ denote time, mass density, velocity fields, magnetic fields, current density, resistivity, and unit vector, respectively. We used the anomalous resistivity in the following form:

$$\eta = 0, \quad (J < J_c), \tag{5}$$

$$\eta = \eta_0 (J/J_c - 1)^2, \quad (J \geqslant J_c), \tag{6}$$

where $J_c = 10^{-9}\,\mathrm{G/cm}$, $\eta_0 = 10^{11}\,\mathrm{cm^2\,s^{-1}}$, and we restrict $\eta \leqslant \eta_{\max} = 10^{11}\,\mathrm{cm^2\,s^{-1}}$.

We inverted velocity fields that reproduce the observational photospheric magnetic fields by solving Equation (3), and we implemented them in the bottom boundary layer of the MHD simulation. The inverted velocity fields were computed by the following three steps:

1. Inversion of the induction equation.

We solved an inverse problem of the induction equation as, in principle,

$$\frac{\boldsymbol{B}_{\mathrm{obs}}^{n+1} - \boldsymbol{B}_{\mathrm{obs}}^{n}}{\tau} = -\nabla \times \boldsymbol{E}^{I}, \tag{7}$$

where $\boldsymbol{B}_{\mathrm{obs}}^{n}$, τ, and $\boldsymbol{E}^{I}$ represent the nth snapshot in the time-series data of the observational magnetic fields, the temporal cadence of the HMI observation, and an inverted electric field, respectively. As pointed out in a previous study (Kusano et al. 2002), we cannot solve this inverse problem completely because Equation (7) includes the derivative in the z-direction (the direction normal to the photosphere), whereas the observational magnetic data have only two-dimensional information in the x-y plane (corresponding to the solar surface). Several methods have been proposed to resolve this problem. In this study, we adopt the poloidal−toloidal decomposition method (Fisher et al. 2010) and obtain $\boldsymbol{E}^{I}$. The advantage of this method is that we can estimate the vertical derivative of electric fields to some extent. However, the complete solution cannot be obtained even by this method. We carried out the inversion of the electric fields between the simulated magnetic fields and the observational magnetic fields during the observational time cadence:

$$\frac{\boldsymbol{B}_{\mathrm{obs}}^{n+1} - \boldsymbol{B}_{\mathrm{sim}}^{n+m/M}}{(1 - m/M)\tau} = -\nabla \times \boldsymbol{E}^{I}, \tag{8}$$

where $\boldsymbol{B}_{\mathrm{sim}}$ denotes the simulated magnetic fields and $m = 1, 2, \ldots, M-1$ represents the mth sub-snapshot between the nth and the $(n+1)$th observational

snapshots. We adopted $M = 6$ in this study; hence, the inversion was performed every 2 minutes during the 12-minute observational cadence of HMI. This piecewise inversion technique increases the feasibility of the observational magnetic fields compared with the case in which electric fields are inverted only once between B_{obs}^{n} and B_{obs}^{n+1}.

2. Gauge transformation.

The electric field is mathematically gauge invariant to the induction equation; we can add an arbitrary scalar potential ϕ in the following form:

$$\boldsymbol{E} = \boldsymbol{E}^{I} - \nabla \phi, \tag{9}$$

where $\boldsymbol{E}$ represents the electric field after gauge transformation. In contrast, as demonstrated by Pomoell et al. (2019), the results of data-driven simulations are influenced by gauge transformation. We adopted a gauge transformation that satisfied $\boldsymbol{E} \cdot \boldsymbol{B} = 0$ using the iterative approach in Fisher et al. (2010). The motivation to use this gauge transformation is as follows: the electric fields defined by $\boldsymbol{E} = -\boldsymbol{v} \times \boldsymbol{B}$ are always perpendicular to magnetic fields. In contrast, the inverted electric fields $\boldsymbol{E}^{I}$ before the gauge transformation usually contain nonzero $\boldsymbol{E}_{\parallel}$ (parallel component to $\boldsymbol{B}$). The nonzero $\boldsymbol{E}_{\parallel}$ can cause a mismatch of the electric fields between the bottom boundary layer and the main simulation domain because the electric fields in the main simulation domain are computed as $\boldsymbol{E} = -\boldsymbol{v} \times \boldsymbol{B}$. Thus, we assumed that $\boldsymbol{E} \cdot \boldsymbol{B} = 0$ is a necessary condition for the boundary electric fields in data-driven MHD simulations. Note that this assumption is valid even if resistive term $\eta \boldsymbol{J}$ was introduced because the magnitude of $\eta \boldsymbol{J}$ is constrained much smaller than that of $-\boldsymbol{v} \times \boldsymbol{B}$ in MHD simulations.

3. Derivation of velocity fields.

We compute velocity fields as follows:

$$\boldsymbol{v}^{I} = \frac{\boldsymbol{E} \times \boldsymbol{B}}{B^2}, \tag{10}$$

where $\boldsymbol{v}^{I}$ represents the inverted velocity field. We substituted $\boldsymbol{B}_{\mathrm{sim}}$ into $\boldsymbol{B}$ in Equation (10). $\boldsymbol{v}^{I}$ was updated every numerical time step.

In step 3, in the case in which $\boldsymbol{E}$ contains $\boldsymbol{E}_{\parallel}$, $\boldsymbol{v}^{I}$ loses the information of $\boldsymbol{E}_{\parallel}$ (because $\boldsymbol{E}_{\parallel} \times \boldsymbol{B} = 0$). In our manipulations, in step 2, $\boldsymbol{E}_{\parallel}$ has already been eliminated by the gauge transformation. The inductive electric fields were calculated in a part of the right-hand side of Equation (3) as follows:

$$\boldsymbol{v}^{I} \times \boldsymbol{B} = \frac{(\boldsymbol{E} \times \boldsymbol{B}) \times \boldsymbol{B}}{B^2} = -\boldsymbol{E} + \frac{(\boldsymbol{E} \cdot \boldsymbol{B})\boldsymbol{B}}{B^2} = -\boldsymbol{E}. \tag{11}$$

Thus, we expect that the observed photospheric magnetic fields are reproduced as a self-consistent numerical solution of Equation (3) only by introducing $\boldsymbol{v}^{I}$ in the bottom boundary. To reduce the observational noise in the area of weak magnetic fields, which can damage the inversion of electric fields and the gauge transformation, we applied a low-pass filter using fast Fourier transform to the original magnetic data. The practical spatial resolution was 8 times lower than the original spatial resolution of the HMI.

The simulation domain is a rectangular box. Its Cartesian coordinates (x, y, z) are extended to $0 < x < 89.6\,\mathrm{Mm}$, $0 < y < 89.6\,\mathrm{Mm}$, and $-1.44\,\mathrm{Mm} < z < 73.8\,\mathrm{Mm}$,

respectively, where the x-y plane is the horizontal plane parallel to the solar surface, and the z-direction represents the height. We adopted uniform grid spacing in every direction, and the grid size was 360 km, corresponding to the spatial resolution of the HMI. Below the $z = 0$ plane, we set five grids in the z-direction where Equation (3) was numerically solved by introducing v^I. Note that only the horizontal derivatives were calculated in the lowest two grids. The $z = -360$ km plane (one grid below $z = 0$) is at the height where the observational magnetic fields were expected to be reproduced. The method of Fisher et al. (2010) derives $\partial_z E_x$ and $\partial_z E_y$. Assuming $\partial_z E_z = 0$, we linearly extrapolated the inverted electric fields in the z-direction below $z = 0$ and computed v^I with the local magnetic fields using Equation (10). The density was fixed to the initial values below $z = 0$. We adopted a free boundary condition in the top boundary and fixed in the side boundaries. Our simulation only included the corona with a typical density of $10^9\,\mathrm{cm}^{-3}$, which is much smaller than the typical photospheric density $10^{17}\,\mathrm{cm}^{-3}$. To suppress the unrealistically fast Alfvèn speed, we reduce the magnetic field strength to be 10 times smaller than the original observed values. The same modification was also adopted in Jiang et al. (2016).

The initial condition was a potential field computed by the Fourier expansion method (Priest 2014) from the vertical magnetic field at 22:58 UT on 2017 November 4, observed by HMI. The initial density was given by $\rho = \rho_0 \exp[-z/H]$, where $\rho_0 = 3.2 \times 10^{-15}\,\mathrm{g\,cm}^{-3}$ and $H = 3.0 \times 10^4$ km. The numerical scheme used was a four-step Runge–Kutta method (Jameson 2017) and a fourth-order central finite difference method with an artificial viscosity (Rempel 2014).

4. Results

Figure 3 shows snapshots of magnetic fields in the bottom boundary at the height $z = -360$ km, where the observed magnetic fields were expected to be reproduced. Note that the magnetic fields shown in Figure 3 are the numerically obtained solutions, not merely smoothed observational data. Compared with Figure 2, we confirmed that the converging motion of the opposite-polarity magnetic patches and the intrusion of the negative patch to the positive patch were well reproduced in our simulation. The small structures were smoothed out by the low-pass filter used for the inversion and the anomalous resistivity during the temporal integration of the MHD simulation. The structural similarity (SSIM) values (Wang et al. 2004) between the raw observational data and the low-pass filtered observational data at $t = 120$ minutes were 0.22, 0.12, and 0.58 for the components B_x, B_y, and B_z, respectively, and the SSIM values between the low-pass filtered observational data and the simulated data were 0.82, 0.61, and 0.93 for the components B_x, B_y, and B_z, respectively. We used the low-pass filtered data for calculation of v^I. We confirmed that the inverted velocities work well because the given magnetic fields were reproduced with high accuracy.

As the opposite-polarity patches converged with each other and the negative magnetic patch further trespassed into the positive magnetic patch, the formation and eruption of flux ropes via reconnection successively occurred in our simulation. Figure 4 shows the temporal evolution of the three-dimensional magnetic field in the corona. Figures 4(a) and (b) show snapshots of when the horizontal magnetic fields were shifted from the potential fields to the observed ones at 22:58 UT on 2017 November 4. Figures 4(c) and (d) show snapshots of the

first eruption. Figures 4(e) and (f) show snapshots of the second eruption. We succeeded in reproducing the successive eruptions of flux ropes. In both cases, the flux ropes erupted in the southwest direction. We can interpret that the erupting filamentary structures in the observation were manifestations of the erupting flux ropes. Compared with Hα blue wing images in the observation (see Figure 1(a3) and (a6)), the directions of eruptions in the simulation were in agreement with the observational results.

Figure 5(a) shows the temporal evolution of the kinetic energy integrated in the simulation domain over the $z = 0$ plane. The rapid increase in kinetic energy at $t \sim 100$ minutes and $t \sim 200$ minutes represents the eruptions. The onset time of the first eruption in the simulation was delayed 40 minutes compared with the observational results, and that of the second eruption was 40 minutes earlier. Figure 5(b) shows the temporal evolution of the nonpotential magnetic energy computed as the difference of the total magnetic energy and the potential magnetic energy. The rapid increase of kinetic energy temporally coincided with the reduction of nonpotential magnetic energy. The kinetic energy was approximately 1×10^{25} erg, and the released magnetic energy was $(2-3) \times 10^{25}$ erg. Note that the magnetic energy can change also as a result of the energy flux at the bottom and the top boundaries. Because we reduced the magnetic field strength in the simulation to 10 times smaller than the original observational values, we can speculate that the actual energy release was of the order of 10^{27} erg for these eruptive events (the right axis of Figure 5(a)). This is because magnetic energy is proportional to B^2, and we solved scale-free MHD equations.

5. Summary and Discussion

We developed a numerical methodology that reproduces the temporal evolution of observational vector magnetic fields in the bottom boundary of MHD simulations by introducing the velocity fields inverted from the time-series observational magnetic data ($\boldsymbol{E} \times \boldsymbol{B}$-driven method). The inverted velocity fields were computed by the formula of $\boldsymbol{E} \times \boldsymbol{B}$ drift. The gauge transformation of the electric field satisfying $\boldsymbol{E} \cdot \boldsymbol{B} = 0$ enables this simple formulation. In the previous data-driven simulations, the velocity fields inferred by DAVE4VM were introduced in addition to the inverted electric fields or the observational magnetic fields (Guo et al. 2019; Hayashi et al. 2019). The DAVE4VM inversely solves the induction equation as well, whereas the vertical derivative of the horizontal components of electric fields is assumed to be negligible. In practice, the observed time evolution of the magnetic fields is not always reproduced completely even if the induction equation was integrated along with the DAVE4VM-inferred velocity fields. Therefore, the previous data-driven simulations used the DAVE4VM-inferred velocity as the bottom boundary condition of the equation of motion and the observational magnetic fields or the inverted electric fields for the induction equation. In the present simulation, the observational magnetic fields were reproduced only by introducing the inverted velocity fields. The bottom boundary condition for the equation of motion and the induction equation is both physically and numerically consistent in our method. We applied our method to the successive eruptive events. Our simulation succeeded in reproducing the successive formation and eruption of flux ropes as a response of temporal evolution of the observational magnetic fields. The inversion technique of electric fields by
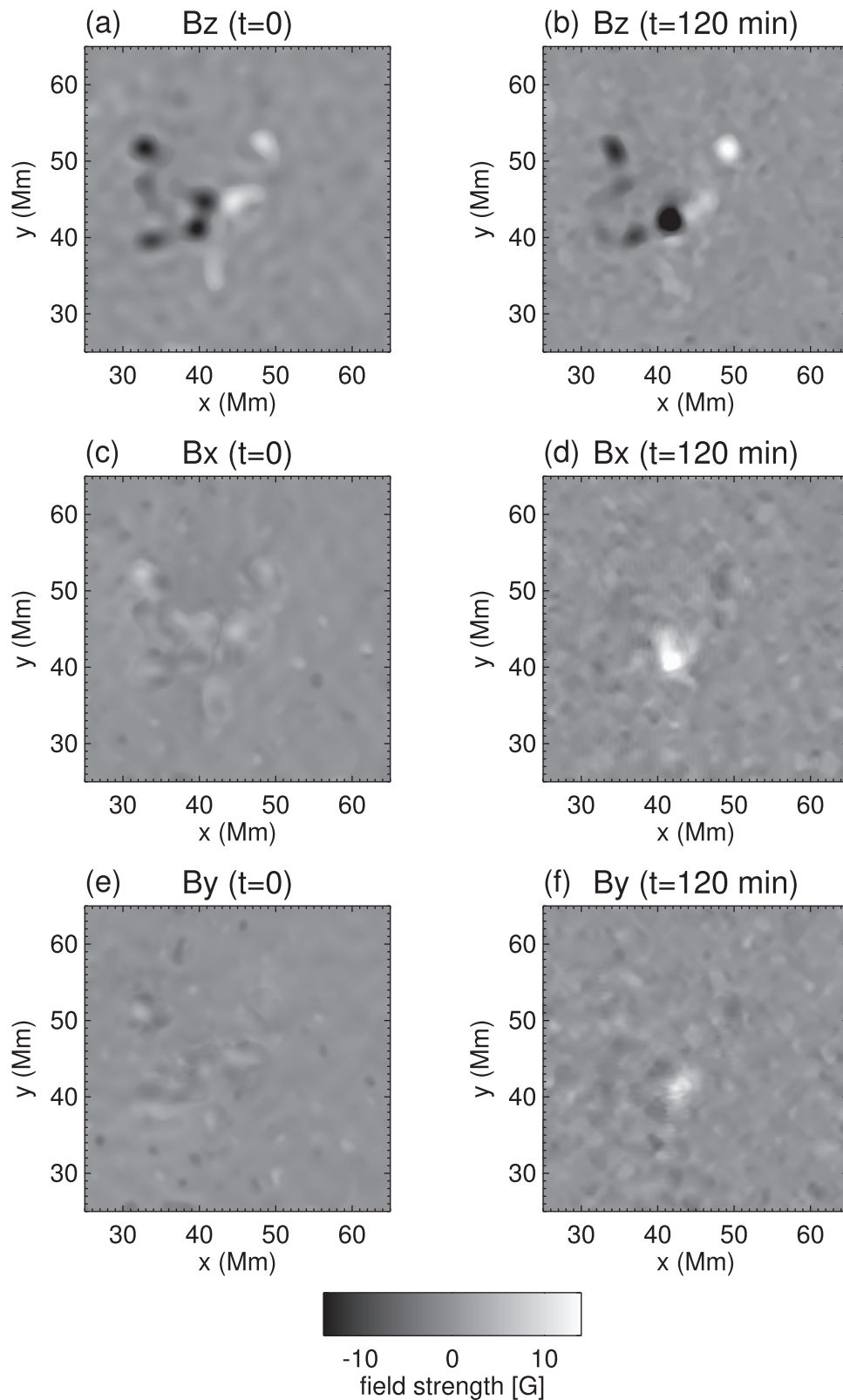
Figure 3. Snapshots of time evolution of magnetic fields at the bottom boundary. Panels (a), (c), and (e) show snapshots of $t = 0$ (corresponding to 2017 November 4, 22:58 UT in the observation). Panels (b), (d), and (f) show snapshots of $t = 120$ minutes (corresponding to 2017 November 5, 0:58 UT in the observation).

Fisher et al. (2010) used in step 1, described in Section 3, was widely used in the previous studies (Pomoell et al. 2019). The computation of the inverted velocity fields in step 3 is straightforward. Our method is simple yet feasible for reproducing magnetic activities in the solar atmosphere.

The energy release of flares in the solar active regions, the typical field strength of which is several thousand gauss, is in
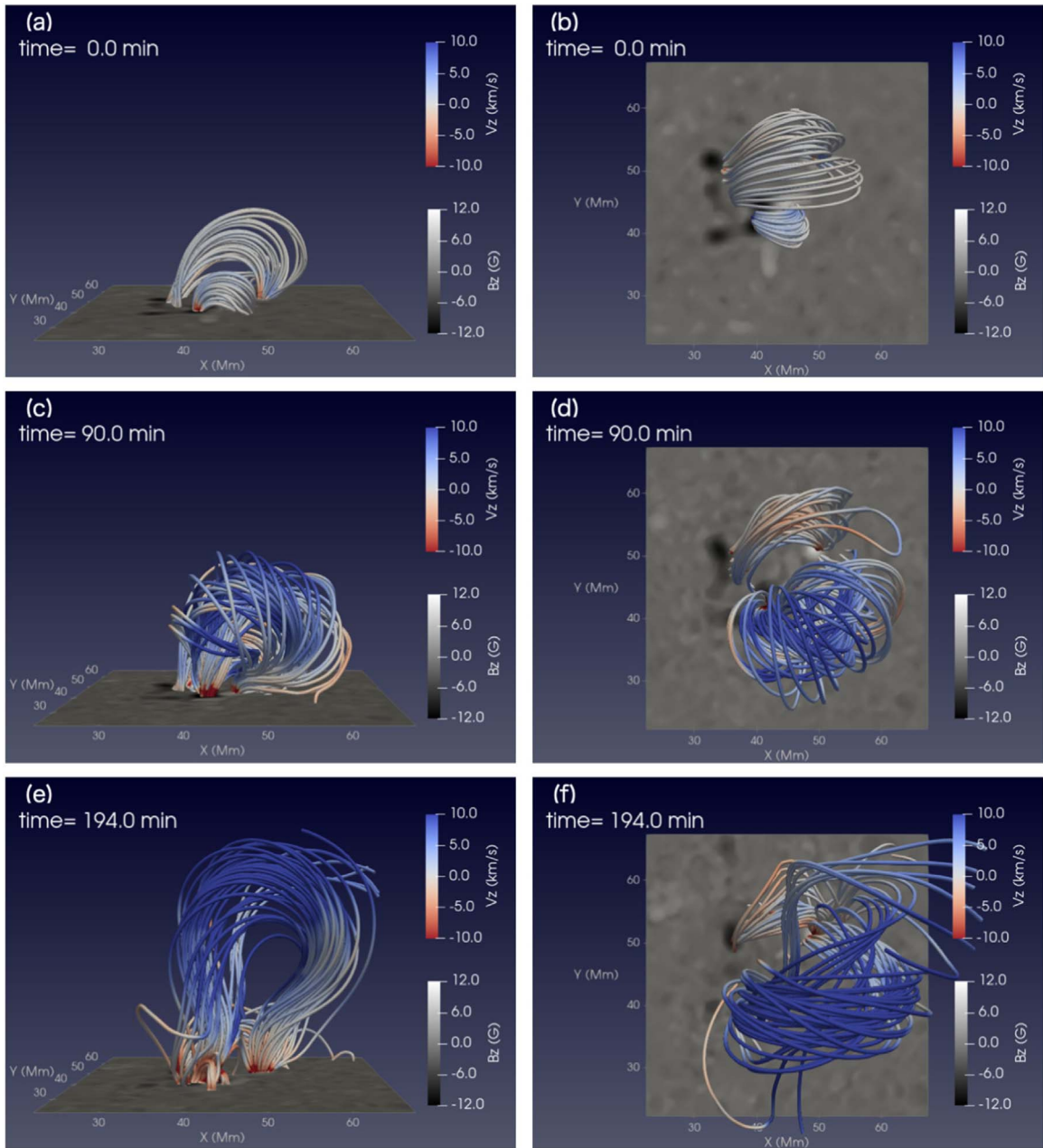
Figure 4. Temporal evolution of the coronal magnetic fields. Lines and colors on the lines represent the magnetic field lines and vertical velocity, respectively. Blue and red represent upward and downward velocities, respectively. The gray scale on the bottom surface represents the vertical magnetic fields. An animation of this figure is available online. The animation runs from $t = -12$ to $+286$ minutes and has a duration of 12 s.

(An animation of this figure is available.)

the range of 10^{28}–10^{32} erg. The field strength of the magnetic patches in our study was ~100 G. The estimation of the released energy of 10^{27} erg from our simulation result is plausible for small eruptive events.

The successive flares and eruptions from active regions are often reported. The largest flare in Solar Cycle 24, which marked X9.3 in the GOES X-ray classification, also had the preceding X2.2 flare. The flares were triggered by the continuous intrusion of the opposite-polarity magnetic fluxes, according to the analyses by Bamba et al. (2020). In our case, although the spatial size and magnetic field strength were much smaller, it is common that the continuous convergence of the opposite magnetic flux and the subsequent partial deformation of the PIL were the triggers of the successive eruptions. It is

worth noting that the triggering mechanism of successive eruptions was similar over a wide range of different spatial and temporal scales. The previous theoretical studies (Kusano et al. 2012, 2020) also support that the partial deformation of PILs can trigger eruption. Kusano et al. (2020) discussed how a small area of reconnection can lead to MHD instability. We speculate that the local converging motion can create small reconnection-favor (opposite-polarity or reversed-shear-type) regions along the PILs in the active regions. In contrast, the origin of continuous converging motion is still unclear. It is also unclear whether the converging motion is concentrated near PILs or ubiquitous in the photosphere. The ultra–high-resolution observations by the Daniel K. Inouye Solar Telescope may reveal this issue. A comprehensive
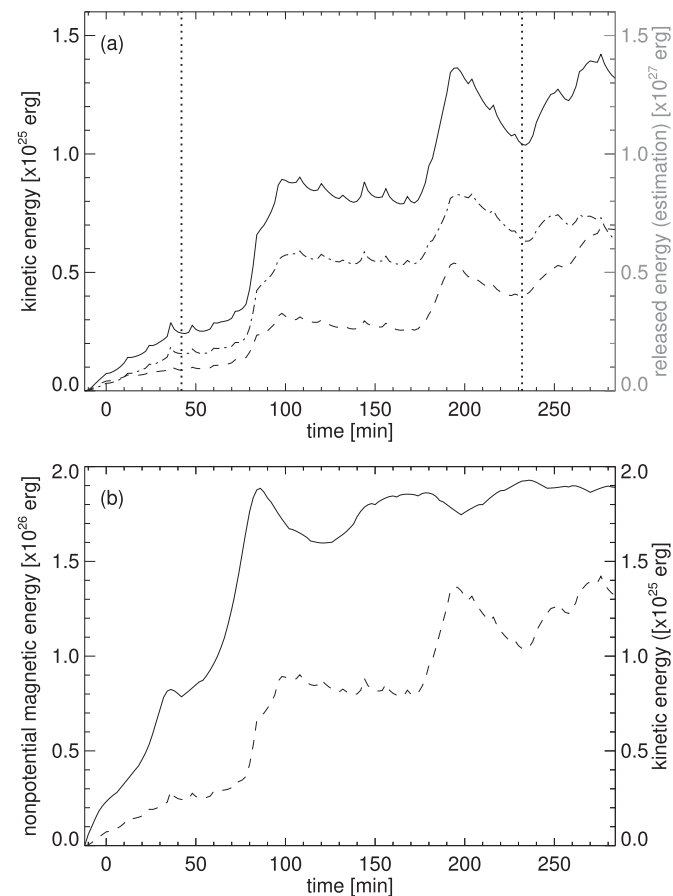
Figure 5. The solid, dashed, and dashed–dotted lines in panel (a) represent the kinetic energy of all velocity components $\int_{z>0}\frac{1}{2}\rho(v_x^2+v_y^2+v_z^2)dV$, of the vertical component $\int_{z>0}\frac{1}{2}\rho v_z^2 dV$, and of the horizontal components $\int_{z>0}\frac{1}{2}\rho(v_x^2+v_y^2)dV$, respectively. The vertical dotted lines indicate the actual onset times of the eruptions in the observation. The right axis in panel (a) represents the estimated released energy in reality. The solid and dashed lines in panel (b) represent the nonpotential magnetic energy and the kinetic energy of all velocity components, respectively.

understanding of the photospheric motion coupling with magnetic activity in the convection zone is also required (Cheung et al. 2019; Hotta et al. 2019; Toriumi & Hotta 2019).

The onset times of the eruptions in our simulations were differed by 40 minutes compared with the observational ones. A possible reason is that the small-scale structures were smoothed out in our simulation. As mentioned in Section 4, the SSIMs of the magnetic fields after applying the low-pass filter were already low. The smaller structures may have to be included as much as possible to reproduce the accurate onset times. The anomalous resistivity might also affect the results. A parameter survey on the anomalous resistivity must be conducted in future work.

ORCID iDs

Takafumi Kaneko ⓘ https://orcid.org/0000-0002-7800-9262
Sung-Hong Park ⓘ https://orcid.org/0000-0001-9149-6547
Kanya Kusano ⓘ https://orcid.org/0000-0002-6814-6810

References

Amari, T., Canou, A., & Aly, J.-J. 2014, Natur, 514, 465
Bamba, Y., Inoue, S., & Imada, S. 2020, ApJ, 894, 29
Chae, J., Wang, H., Lee, C.-Y., Goode, P. R., & Schühle, U. 1998, ApJL, 504, L123
Cheung, M. C. M., De Pontieu, B., Tarbell, T. D., et al. 2015, ApJ, 801, 83
Cheung, M. C. M., & DeRosa, M. L. 2012, ApJ, 757, 147
Cheung, M. C. M., Rempel, M., Chintzoglou, G., et al. 2019, NatAs, 3, 160
Fisher, G. H., Welsch, B. T., Abbett, W. P., & Bercik, D. J. 2010, ApJ, 715, 242
Guo, Y., Xu, Y., Ding, M. D., et al. 2019, ApJL, 884, L1
Hayashi, K., Feng, X., Xiong, M., & Jiang, C. 2018, ApJ, 856, 181
Hayashi, K., Feng, X., Xiong, M., & Jiang, C. 2019, ApJL, 871, L28
He, W., Jiang, C., Zou, P., et al. 2020, ApJ, 892, 9
Hood, A. W., & Priest, E. R. 1979, SoPh, 64, 303
Hotta, H., Iijima, H., & Kusano, K. 2019, SciA, 5, 2307
Ichimoto, K., Ishii, T. T., Otsuji, K., et al. 2017, SoPh, 292, 63
Inoue, S. 2016, PEPS, 3, 19
Ishiguro, N., & Kusano, K. 2017, ApJ, 843, 101
Jameson, A. 2017, AIAAJ, 1487
Jiang, C., Wu, S. T., Yurchyshyn, V., et al. 2016, ApJ, 828, 62
Kliem, B., & Török, T. 2006, PhRvL, 96, 255002
Kusano, K., Bamba, Y., Yamamoto, T. T., et al. 2012, ApJ, 760, 31
Kusano, K., Iju, T., Bamba, Y., & Inoue, S. 2020, Sci, 369, 587
Kusano, K., Maeshiro, T., Yokoyama, T., & Sakurai, T. 2002, ApJ, 577, 501
Maehara, H., Shibayama, T., Notsu, S., et al. 2012, Natur, 485, 478
Muhamad, J., Kusano, K., Inoue, S., & Shiota, D. 2017, ApJ, 842, 86
Namekata, K., Maehara, H., Sasaki, R., et al. 2020, PASJ, 72, 68
Notsu, Y., Maehara, H., Honda, S., et al. 2019, ApJ, 876, 58
Osten, R. A., Hawley, S. L., Allred, J. C., Johns-Krull, C. M., & Roark, C. 2005, ApJ, 621, 398
Pandey, J. C., & Singh, K. P. 2008, MNRAS, 387, 1627
Pesnell, W. D., Thompson, B. J., & Chamberlin, P. C. 2012, SoPh, 275, 3
Pomoell, J., Lumme, E., & Kilpua, E. 2019, SoPh, 294, 41
Priest, E. 2014, Magnetohydrodynamics of the Sun (Cambridge: Cambridge Univ. Press)
Rempel, M. 2014, ApJ, 789, 132
Schou, J., Scherrer, P. H., Bush, R. I., et al. 2012, SoPh, 275, 229
Schuck, P. W. 2006, ApJ, 646, 1358
Toriumi, S., & Hotta, H. 2019, ApJL, 886, L21
Toriumi, S., Takasao, S., Cheung, M. C. M., et al. 2020, ApJ, 890, 103
UeNo, S., Nagata, S.-i., Kitai, R., Kurokawa, H., & Ichimoto, K. 2004, Proc. SPIE, 5492, 958
Wang, H., Johannesson, A., Stage, M., Lee, C., & Zirin, H. 1998, SoPh, 178, 55
Wang, Z., Bovik, A. C., Sheikh, H. R., & Simoncelli, E. P. 2004, ITIP, 13, 600